Development of satellite green vegetation fraction time series for use in mesoscale modeling

application to the European heat wave 2006

Boegh, Eva; Nielsen, Joakim Refslund; Dellwik, Ebba; Hahmann, Andrea N.; Barlage, Michael J.

Published in:
Theoretical and Applied Climatology

DOI:
10.1007/s00704-013-1004-z

Publication date:
2014

Document Version
Early version, also known as pre-print

Citation for published version (APA):
Boegh, E., Nielsen, J. R., Dellwik, E., Hahmann, A. N., & Barlage, M. J. (2014). Development of satellite green vegetation fraction time series for use in mesoscale modeling: application to the European heat wave 2006. *Theoretical and Applied Climatology*, *117*(3-4), 377-392. https://doi.org/10.1007/s00704-013-1004-z

Theor Appl Climatol
DOI 10.1007/s00704-013-1004-z

ORIGINAL PAPER

Development of satellite green vegetation fraction time series for use in mesoscale modeling: application to the European heat wave 2006

Joakim Refslund · Ebba Dellwik · Andrea N. Hahmann · Michael J. Barlage · Eva Boegh

Received: 8 November 2012 / Accepted: 27 August 2013

Abstract A method is presented for development of satellite green vegetation fraction (GVF) time series for use in the Weather Research and Forecasting (WRF) model. The GVF data is in the WRF model used to describe the temporal evolution of many land surface parameters, in addition to the evolution of vegetation. Several high-resolution GVF products, derived from high-quality satellite retrievals from Moderate Resolution Imaging Spectroradiometer images, were produced and their performance was evaluated in long-term WRF simulations. The atmospheric conditions during the 2006 heat wave year over Europe were simulated since significant interannual variability in vegetation seasonality was found. Such interannual variability is expected to increase in the coming decades due to climatic changes. The simulation using a quadratic normalized difference vegetation index to GVF relationship resulted in consistent improvements of modeled temperatures. The model mean temperature cold bias was reduced by 10 % for the whole domain and by 20–45 % in areas affected by the heat wave. The study shows that WRF simulations during heat waves and droughts, when vegetation conditions deviate from the climatology, require concurrent land surface properties in order to produce accurate results.

J. Refslund (✉) · E. Dellwik · A. N. Hahmann
DTU Wind Energy, Technical University of Denmark,
Frederiksborgvej 399, 4000 Roskilde, Denmark
e-mail: jref@dtu.dk

M. J. Barlage
Research Application Lab, NCAR, Boulder, CO, USA

E. Boegh
Roskilde University, Roskilde, Denmark

1 Introduction

The presence of vegetation influences weather and climate through its modification of the energy and water exchange across the land–atmosphere boundary. Partitioning of net solar radiative energy into sensible, latent, and ground heat fluxes affects moisture and temperature fields, which in turn can alter the structure of the planetary boundary layer (PBL) leading to changes in cloud cover and rainfall and to the development of thunderstorms (Stull 1988; Pielke 2001; Pielke et al. 2007; Montandon et al. 2011). Conversely, longer-term meteorological conditions and persistent climatic changes influence the distribution of vegetation, for example by exposing them to stresses related to excessive heat and drought.

For Europe, climate change studies have shown that the occurrence of heat waves and above-average high temperatures in the summer months will increase during the coming decades leading to dryer summer conditions (Teuling et al. 2010; Seneviratne et al. 2006) and, consequently, to changes in land cover characteristics through altered vegetation seasonalities. The predictions have been supported by at least three summer heat waves during the last decade, in August 2003, in July 2006, and in June and July 2010. The periods were associated with widespread impact on human mortality, ecosystem damages and crop failures, water shortages, and severe thunderstorm development (Teuling et al. 2010; Della-Marta et al. 2007).

The land cover characteristics used in regional weather prediction and climate models can be represented and derived in several ways. The Noah land surface model (LSM) coupled to the Weather Research and Forecasting (WRF) model uses green vegetation fraction (GVF) as a tool to represent vegetation seasonalities (Skamarock et al. 2008). The horizontal distribution of vegetation canopies is

Published online: 20 September 2013

directly represented by GVF, whereas the leaf area index (LAI), which is linearly scaled within a certain range using GVF, describes its vertical thickness in each grid cell. The values of surface albedo, emissivity, and roughness are scaled in a similar fashion. Thus, the surface energy calculations in the Noah LSM are critically dependent on the GVF data.

The GVF climatology typically used in the Noah LSM was derived from normalized difference vegetation index (NDVI) composites obtained by the Advanced Very High Resolution Radiometer (AVHRR) during 1985–1991. Monthly global NDVI images with grid spacing of 0.144°, produced from averaged weekly composites subjected to spatial smoothing for cloud reduction and for gap filling purposes, were converted into GVF using a linear approach (Gutman and Ignatov 1998; Jiang et al. 2010). The default climatology has been successfully applied in forecast and climate studies but possesses obvious limitations. For instance, the inherent low spatial resolution may reduce accuracy of high-resolution simulations, while land cover alterations of weekly or biweekly scale are not captured by the temporal resolution (Hong et al. 2009; Jiang et al. 2010). Additionally, impacts from interannual variability, changes in management practices, and recent climatic changes are not reflected in the data.

Land cover information derived from Moderate Resolution Imaging Spectroradiometer (MODIS) NDVI data has recently been applied in studies using the Noah LSM. Miller et al. (2006) used a linear method (Zeng et al. 2000) to compute monthly GVF data from a quality improved 2002 NDVI product (Moody et al. 2005). They compared vegetation seasonalities to the AVHRR GVF climatology for the Continental United States and found improved seasonality for evergreen needleleaf forest and more realistic summer values for grassland. However, too high GVF values were found during the wintertime for deciduous and mixed forests, grasslands, and croplands. Hong et al. (2009) and Lakshmi et al. (2011) investigated the impact of different MODIS 2002 GVF representations in high-resolution short-term coupled WRF/Noah simulations at 1-km^2 grid spacing to quantify the modeled energy and water response. They derived NDVI from 8-day MODIS reflectance data, replacing cloud contaminated pixels with a null value, and assumed both linear and quadratic NDVI relationships to GVF. Numerical predictions were compared to observations obtained during the 2002 International H_2O Project (Weckwerth et al. 2004). Their investigations did not result in clear recommendations to whether the linear or quadratic relation should be used concerning the WRF model.

A short-term simulation with high spatial resolution is not sufficient to evaluate the performance of a new high-resolution GVF product in the WRF model. Evaluation must be done across spatial scales, due to the nesting capability and during different periods in the annual cycle. A year with large interannual variability is suitable for such investigation since the performance of the product is challenged to its maximum. Here, a thorough investigation of the use of high-resolution MODIS GVF in the WRF model is carried out using simulations of the 2006 heat wave year over Europe.

The objective of this study is twofold: (1) to quantify whether a linear or a quadratic MODIS NDVI to GVF relation is more suitable for WRF/Noah simulations and (2) to investigate the impact of concurrent land cover information in WRF/Noah simulations both during heat wave events, where changes are expected to be significant, and during periods where impacts are expected to be minor. These aims are achieved in three steps. First, we develop a new statistically robust filled MODIS NDVI climatology, reflecting impacts from recent landuse and climatic changes over Europe. High quality is ensured through an extensive post-processing procedure that includes a combination of existing methods and novel data-processing ideas. Second, a comparison of the annual variation of GVF for various landuse classes is carried out at a grid spacing that is close to the best resolution offered by the AVHRR GVF data. Third, several climate simulations using different GVF representations in WRF/Noah, including the AVHRR GVF data, are compared to gridded temperature data to assess model performances.

The paper is structured as follows: In Section 2, we introduce the NDVI climatology procedure and the methods used to obtain the final MODIS GVF products. Model setup and verification data are described in Section 3, followed by comparisons of the different vegetation seasonalities in Section 4. Results from climate simulations are presented in Section 5 and, finally, we discuss and conclude our findings in Sections 6 and 7.

2 Green vegetation fraction data

2.1 Input data

We selected the MODIS instrument aboard the polar-orbiting *Aqua* and *Terra* satelittes as our data source. The NDVI level-3 products (MOD13A2 and MYD13A2, Version-5) are composited every 16 days at 1-km^2 resolution on a tiled Integerized Sinusoidal (IS) 10° grid, with each tile covering 1,200 × 1,200 km. The data sets are produced with an offset of 8 days to improve the temporal frequency, such that the starting period is days 001 and 009 of *Terra* and *Aqua*, respectively. We use 10 years of data from *Terra*, 2001–2010, and 9 years from *Aqua* starting from year 2002 day 185 and ending at year 2011 day 169. To cover the majority of Europe, we gathered nine tiles for each 8-day period and reprojected the data

into geographic coordinates using the MODIS Reprojection Tool developed by NASA Land Processes Distributed Active Archive Center (LP DAAC). The resultant latitudinal coverage ranges from 40°N to 70°N, whereas the longitudinal coverage ranges from 13°W to 26°E in the south and from 29°W to 58.5°E in the north. The quality control (QC) information for each pixel is stored as 16-bit data that can easily be accessed. We use the MODIS land cover product (MOD12Q1, Type 1) containing the International Geosphere-Biosphere Programme (IGBP) land cover classification, including 11 natural vegetation classes, 3 developed and mosaicked land classes, and 3 non-vegetated land classes (Friedl et al. 2002), to assign each pixel with a landuse class. The southern regions in Europe are usually well represented in the NDVI images even during wintertime, except for the Alps and the Pyrenees, while the most northern areas, approximately above 60°N, only have valid retrievals for a few months during the summer. The entire domain consists of 49.2 % water and 50.8 % land pixels with more than 75 % represented in four major land classes: croplands (28.5 %), evergreen needleleaf forest (21.4 %), mixed forest (16.4 %), and open shrubland (10.8 %).

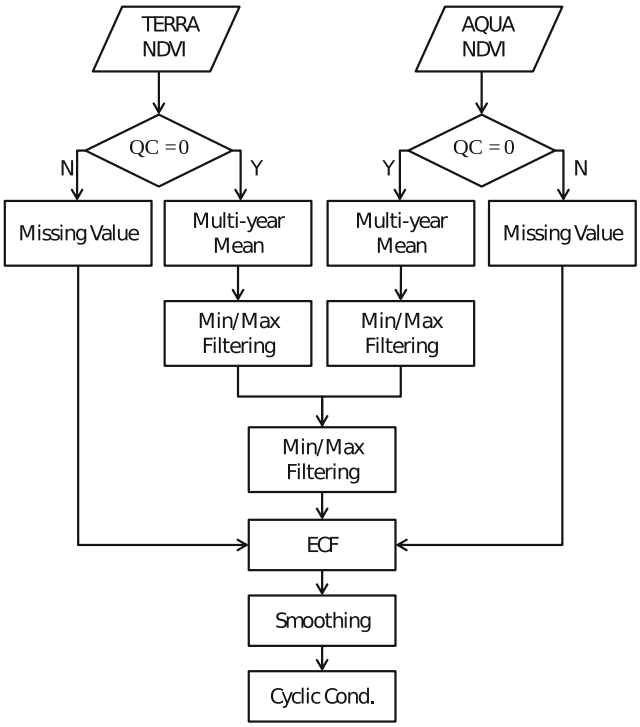

Fig. 1 Flowchart outlining the reconstruction process of the multiyear MODIS NDVI climatology

2.2 Method

Although algorithms to retrieve high-quality MODIS NDVI data have improved over the recent years, noise related to clouds, snow cover, and aerosols still remains (Didan and Huete 2006). Typically, noise generates significantly lower NDVI values that lead to unrealistic time series, inconsistent with the relatively slow growth and decay of the vegetation. Several noise-reduction methods have been suggested to derive high-quality smooth NDVI time series (Viovy et al. 1992; Verhoef et al. 1996; Roerink et al. 2000; Lovell and Graetz 2001; Jonsson and Eklundh 2002; Chen et al. 2004; Moody et al. 2005; Ma and Veroustraete 2004; Gu et al. 2009), but the optimal approach depends on the use of the data since no method is free of drawbacks.

We chose to use only the highest-quality NDVI data to minimize noise in the time series. Therefore, a filled NDVI climatology was assessed as an optimal method for gap filling of single-year time series. To derive a filled NDVI climatology, we adopted the idea of ecosystem-dependent filling (ECF) (Moody et al. 2005) but combined our procedure with (1) a multiyear averaged background field, (2) a local minimum and maximum correction filter to remove unrealistic average values, and (3) a simple three-point smoothing technique also applied by Gu et al. (2009). Additionally, we applied a cyclic condition filter to avoid large jumps at the December–January transition. The climatology process is described in the next four sections and additionally depicted in the flowchart in Fig. 1.

2.2.1 Multiyear average

A multiyear average for each 16-day composite was calculated from *Aqua* and *Terra* data inspired by Yuan et al. (2011). The procedure counts the number of available values in each pixel during the 9 or 10 years and compute the mean value if two conditions are met. First, only pixel values with the highest-quality flag (QC=0) are considered and, second, at least three pixel values are available for the averaging; otherwise, the mean is represented by a missing value. The conditions ensure that each mean value represents a "true" background value with minimal influence from noise-affected values.

2.2.2 Local minimum/maximum filter

The above approach does not prevent noise in the discontinuous multiyear averages, especially in northern latitudes and during the winter months. Thus, we applied an intelligent local minimum/maximum filter to remove unrealistic values in the time series. Initially, the filter identifies local minimum/maximum values associated with gradients larger than 0.2/16 days. Then, gradients between four adjacent data points, centered around the local minimum/maximum value, are examined and a decision on which value to remove is made. This decision is based on two conditions: (1) the

value of the data point has to be a local minimum or maximum and (2) the gradients must have the highest combined absolute gradient. The gradient threshold of 0.2 was selected after careful heuristic considerations.

Initially, the *Aqua* and *Terra* time series were processed separately to minimize the impacts from mistakes done by the filter that potentially could be compensated for by combining the time series as shown in Fig. 1. By mistakes, we here refer to errors which are obvious to the human eye but invisible to the filter. The procedure was repeated on the combined *Aqua* and *Terra* time series using a threshold of 0.1/8 days. An example is shown in Fig. 2. The filter recognizes the encircled values as unrealistic and remove these before filling and smoothing algorithms are applied to the time series.

2.2.3 Filling and smoothing

We applied a simple ecosystem-dependent filling technique to remove missing values in the climatological time series. The method represents the ensemble phenological behavior for each landuse class as the median of all available values for each temporal period within three zonal regions spanning 10° (40°–50°, 50°–60°, and 60°–70°). The relatively large zones ensure that the phenology curves are produced from enough values while allowing significant latitudinal variations for each vegetation class.

The derived ensemble phenology curves are subsequently smoothed with a simple three-point smoothing algorithm:

$$N_{\mathrm{se}}(t) = \frac{1}{2}N_{\mathrm{e}}(t) + \frac{1}{4}\left[N_{\mathrm{e}}(t-1) + N_{\mathrm{e}}(t+1)\right] \qquad (1)$$

to avoid jigsaw-like features especially during the winter months. The subscripts "se" and "e" indicate smoothed and raw ensemble values, respectively, while t indicates time and N is short for NDVI.

For gap filling of the multiyear average time series, we applied the smoothed, ensemble phenology curve trends instead of actual values, assuming that the majority of pixels within the same landuse class and region show the same phenological pattern. The method requires that at least one value in the individual time series exists. The filling is done in several steps. Initially, both backward filling and forward filling are attempted starting from day 201 towards either day 001 or 361. Afterwards, filling from day 001 to day 361 and backwards is done to fill values that were not filled in the first pass. The method ensures that potential jumps from filling only occur during the December–January transition and that areas with very little information about the vegetation seasonality, such as the mountainous regions in the Alps and Pyrenees and northern Scandinavia, obtain full phenology curves based on the ensemble mean seasonalities. After the filling, we applied the smoothing procedure on all of the pixel time series. The final appearance of a randomly selected climatological curve (solid) after filling and smoothing has been applied to the initially discontinuous NDVI multiyear average (dashed) as shown in Fig. 2.

2.2.4 Cyclic conditions

We used a linear algorithm to ensure cyclic conditions at the December–January transition only allowing gradients less or equal to 0.1/8 days. The cyclic filter was particularly in use above 60°N, where vegetation impacts on modeling results anyway are minimal due to low radiation and persistent snow cover conditions. If a gradient larger than 0.1 and less than 0.2 was detected, a linear interpolation between day 361 and day 33 replaced the original phenology curve. For intervals larger than 0.2, we set the December–January transition to 0.1 and scaled the remaining values linearly between days 1 and 33. The procedure was selected in order to maintain the curve minimum in the February–March period, as is typically observed for the region. Finally, pixels solely consisting of missing values were assigned with smoothed ensemble phenology curves matching the pixel landuse class and zone. Less than 0.0002 % of the pixels were filled in this manner.

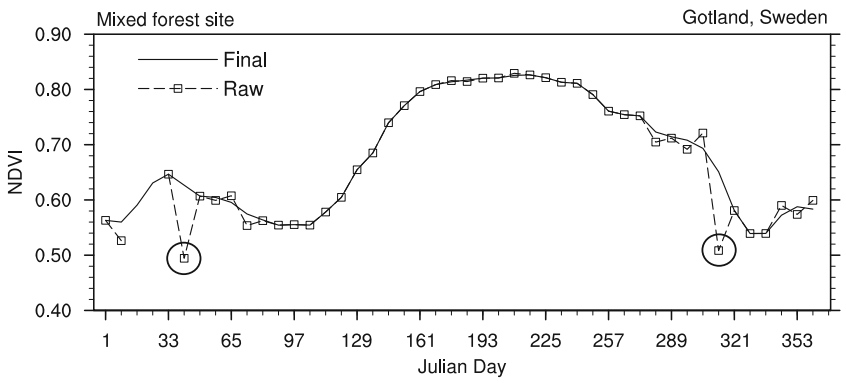

Fig. 2 Time series of NDVI from a pixel located on the island of Gotland, Sweden. The raw multiyear average is indicated by the *dashed marked line* and the final NDVI climatology by *solid line*. *Enclosed circles* are identified as unrealistic values

2.2.5 Single-year representation

Since we can exploit the added pixel-level information provided by the climatology, the procedure to obtain an explicit filled 2006 NDVI time series (or any year) is much simpler than for the multiyear climatology. As before, we only use good-quality data (QC=0) from 2006 but neglect the local correction as applied for the climatology. Gap filling is performed with trends from the climatological time series and is thus primarily based on pixel-level phenology curves and not on zonally averaged ecosystem-dependent curves. Finally, the smoothing algorithm was applied to the specific 2006 NDVI values.

2.2.6 Derivation of green vegetation fraction

The NDVI climatology or the annually filled representation of NDVI can be converted into GVF in several ways using

$$\mathrm{GVF} = \left(\frac{N - N_\mathrm{s}}{N_\mathrm{v} - N_\mathrm{s}}\right)^p \tag{2}$$

where N represents the time-varying NDVI value at each grid cell, N_v and N_s represent NDVI values at full green vegetation cover and at bare soil, respectively, and p is a constant. We use the method described by Zeng et al. (2000) where N_v is considered a function of vegetation type and both N_v and N_s are varying within each year. Since we consider a limited area, N_s is regionally defined and computed to $N_\mathrm{s} \approx 0.05$ for all data sets. N_v was found to vary between 0.75 and 0.90 with slightly higher values in the 2006 specific NDVI time series. The calculated values are close to what others have found (Montandon and Small 2008).

The AVHRR GVF data was obtained using the linear approach and by assuming N_v and N_s as spatially and temporally constant values. The NDVI values were globally defined and estimated to $N_\mathrm{v} = 0.52$ and $N_\mathrm{s} = 0.04$ (Gutman and Ignatov 1998). We decided to test both the linear and the quadratic formulation for our single-year representations.

3 Model and verification data

3.1 Numerical model

We used the WRF Advanced Research (ARW) model version 3.3.1 maintained by the National Center for Atmospheric Research for our numerical simulations (Skamarock et al. 2008). An overview of the selected physical parameterizations as well as forcing data is given in Table 1.

Sea surface temperatures are described by the Optimum Interpolation Sea Surface Temperature (OISST) at 0.25° grid spacing and daily resolution. Initial and lateral boundary conditions are obtained from the Climate Forecast System Reanalysis (CFSR) data at 0.5° horizontal resolution made available by the National Centers for Environmental Prediction (NCEP). Grid nudging from the Four-Dimensional Data Assimilation (FDDA) system is used on temperature, moisture, and wind components above the lowest 15 model levels, but excluded within the PBL for temperature and moisture. The nudging technique ensures that upper-air model predictions do not drift too far away from the reanalysis conditions. We use 41 vertical levels and horizontal grid intervals of 18 km.

Table 1 Overview of the physical packages and forcing data used in our simulations

	Name	Reference
Parameterization		
Land surface	Noah	Chen and Dudhia (2001)
Surface layer	Eta	Janjic (1996)
Planetary boundary layer	MYJ	Janjic (2002)
Longwave radiation	RRTM	Mlawer et al. (1997)
Shortwave radiation	Duhia	Dudhia (1989)
Microphysics	WSM5	Hong et al. (2004)
Cumulus	Kain-Fritsch	Kain (2004)
Forcing data		
Initial and boundary	CFSR	Saha et al. (2010)
Land surface spin-up	GLDAS	Chen et al. (2007)
Sea surface state	OISST	Reynolds et al. (2007)
Grid nudging	q,T,u,v	Stauffer and Seaman (1990)

The High-Resolution Land Data Assimilation (HRLDAS) system (Chen et al. 2007) was used for initial spin-up of soil moisture and soil temperature. The HRLDAS system was adapted to use 3-hourly Global Land Data Assimilation System (GLDAS) data and ran for a period of 2 years prior to simulation start, on 1 January 2006. The HRLDAS system used the Noah LSM with the AVHRR GVF data and all runs were initialized with the predicted soil state.

The IGBP land cover distribution and the extent of our computational domain are shown in Fig. 3. The 1-km grid spacing of the land cover data was interpolated by the WRF Preprocessing System (WPS version 3.3) (Skamarock et al. 2008) to 18 km using the dominant vegetation type to determine the classification at each pixel. Thus, 91.5 % of all pixels belong in four land cover classes: 39.6 % water, 26.4 % croplands, 15.1 % mixed forest (MF), and 10.4 % evergreen needleleaf forest (ENF). ENFs are mainly defined to northern areas such as Sweden, Norway, and Finland while MFs are found in areas such as the Baltics, Scotland,

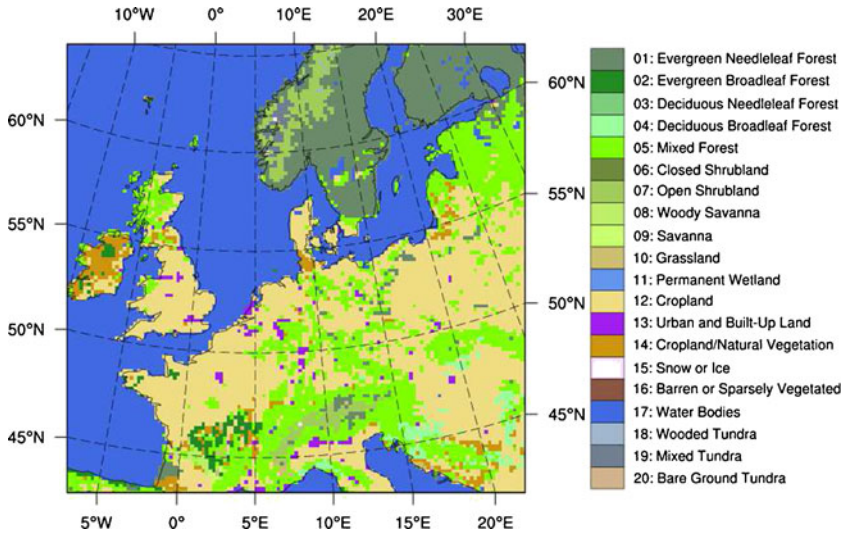

Fig. 3 IGBP landuse classes in the 18-km WRF domain

Germany, Slovakia, and near the Alps. Croplands mainly exist south of 58°N.

The MODIS GVF data, described in Section 2, were linearly interpolated into daily files and, additionally, fields with yearly minimum and maximum vegetation fractions were computed. The latter files are important for correct scaling of LAI, roughness, emissivity, and albedo and are different for each version of the GVF data. The WPS system horizontally interpolated all fields to 18-km grid spacing to preserve consistency with the interpolated IGBP land cover data. The WRF model was adapted to use the new GVF files.

3.2 E-OBS and GPS data

To validate the model performances, we used the European daily high-resolution gridded data set (E-OBS, v5.0) developed for climate change studies and for validation of regional climate models (Haylock et al. 2008). It is based on the European Climate Assessment and Data network of measuring stations (ECA&D) and include minimum, maximum, and mean daily 2-m temperature, as well as daily precipitation. The mean daily 2-m temperature in E-OBS is calculated as the average of the maximum and minimum daily temperatures obtained as being the most extreme values at hour 00, 06, 12, or 18. About 2,000 stations were used for developing E-OBS with the highest station densities found in the UK, Benelux, and the Alps.

Several issues with E-OBS have been identified by comparison to observational data sets with higher station density (Hofstra et al. 2009; Kyselý and Plavcová 2010). The main problems are related to the interpolation of station measurements in areas with limited station density or in complex terrain, where the station measurements are not representative of their surroundings. For instance, Kyselý and Plavcová (2010) found that temperature extremes in the Czech Republic were substantially underestimated in E-OBS with cold extremes being too warm and warm extremes being too cold. The interpolation procedure results in regional biases in both temperature and precipitation and is particularly severe for extreme values. Despite these problems, E-OBS was considered the best solution for verification of our numerical simulations.

In addition to E-OBS, we use precipitable water data measured by a permanent GPS station, PTBB, located in central Germany (Braunschweig, Niedersachsen) to verify temporal variations in water vapor in the WRF model simulations (Bruyninx 2004).

4 Seasonality comparison

Vegetation seasonalities for forest types represented in the WRF domain are shown in Fig. 4. In addition to ENF and MF that were defined in Section 3.1, we use EBF and DBF as abbreviations for evergreen broadleaf forest and deciduous broadleaf forest, respectively. The AVHRR GVF climatology and the MODIS GVF climatology are indicated by Clim-A and Clim-M, respectively, while the linear and quadratic single-year MODIS GVF products are indicated by 2006-L and 2006-Q, respectively.

Large differences in the representations of vegetation fraction for ENF are shown in Fig. 4(a). Clim-M, 2006-L, and 2006-Q show higher vegetation fractions during the whole annual cycle compared to Clim-A, with the highest values indicated by the linear methods. The vegetation fractions of Clim-M and 2006-L are in the range of 50–90 %, while Clim-A and 2006-Q are in the range of 5–70 and

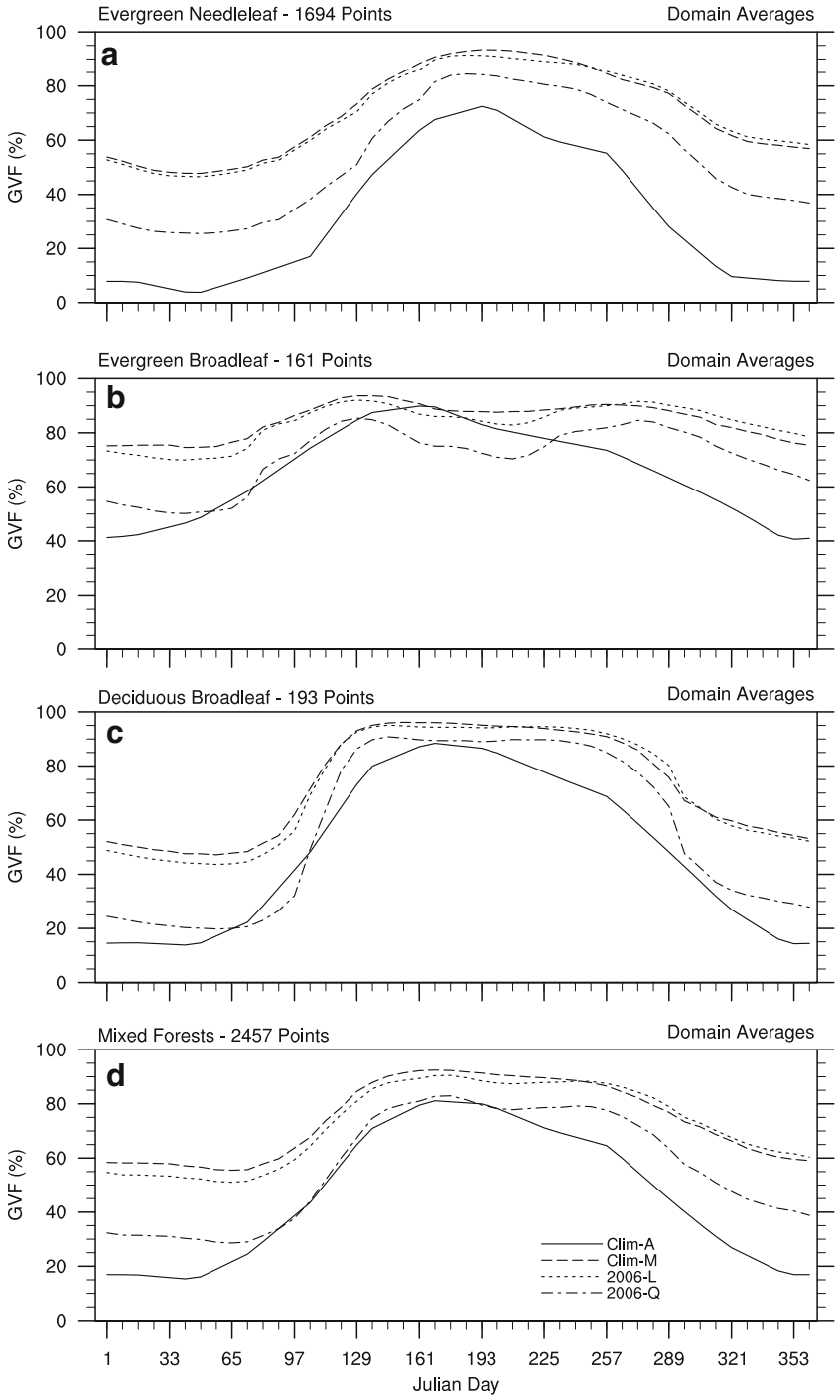

Fig. 4 Comparison of domain-averaged GVF (in percent) for (*a*) ENF, (*b*) EBF, (*c*) DBF, and (*d*) MF at 18-km resolution. *Solid lines* represent Clim-A and the *long dashed*, *short dashed*, and *long-short dashed lines* represent Clim-M, 2006-L, and 2006-Q, respectively

25–85 %, respectively. The intraannual variability between all representations is similar indicating that figures with LAI, roughness, emissivity, and albedo will be very similar as well (not shown).

Vegetation fractions for EBF are shown in Fig. 4(b). Clim-M and 2006-L show little annual variation ranging from 70 to 90 %, while Clim-A and 2006-Q indicate larger variations of 40–90 and 50–85 %, respectively. A decrease in GVF during June–July followed by an increasing trend during August–September for all MODIS data is not observed in Clim-A. The majority of EBF sites are located in southern France (see Fig. 3), a region that was also severly affected by the heat wave 2003 (Rebetez et al. 2009). The difference in intraannual variability reflects stresses on EBF due to heat and drought conditions. Due to scaling of the LAI table values, the GVF variability is also

reflected in LAI where Clim-A shows higher summer values compared to those derived from the MODIS data. The opposite occur in the autumn where lower LAI values are found in Clim-A (not shown).

Figure 4(c, d) shows vegetation seasonalities for DBF and MF. Clim-M and 2006-L show the highest values while Clim-A and 2006-Q compare well in terms of maximum and minimum vegetation fraction. Summer values are in the range of 75–95 %, while winter and late autumn values range between 15 and 60 %, with lowest values shown by Clim-A and 2006-Q. Clim-A shows slowly evolving vegetation cover for DBF while more rapid growth and decaying trends are shown by Clim-M, 2006-L, and 2006-Q. Additionally, a prolonged growth period (April–October) for both DBF and MF is indicated in the GVF data derived from MODIS compared to Clim-A.

The seasonal evolution of GVF for open shrublands (OS), cropland/natural vegetation (CN), and croplands (CL) together with LAI, roughness, and emissivity for CL is shown in Fig. 5(a–f). The intraannual variability for OS is very similar between all GVF representations with the highest fractions shown by Clim-M and 2006-L (Fig. 5(a)). This is somewhat misleading since OS show significant latitudinal dependency. The MODIS-derived GVF data results in higher vegetation fractions over Scandinavia compared to Clim-A during the entire annual cycle, while Clim-A shows higher summer vegetation fraction over the Alps and slightly lower during the winter (not shown).

Figure 5(b) shows vegetation fractions representing CN but indicates very similar development to MF shown in Fig. 4(d). It reflects that the majority of CN sites are located in the vicinity of MFs while points classified as CN but surrounded by CL resemble the vegetation seasonality of CL better (not shown).

Vegetation fractions indicating CL seasonalities are shown in Fig. 5(c). Higher values are consistently shown by Clim-M and 2006-L compared to Clim-A and 2006-Q and range between 50 and 90 %, while a range of 15–75 % is shown by Clim-A and 2006-Q. Clim-A and 2006-Q compare well during the first half seasonal cycle, but show significant difference in seasonal development during the last part of the year. A large decrease in GVF during June–July is shown by 2006-Q compared to the climatologies indicating either early harvesting or stresses related to drought and excess temperature. 2006-Q shows a decrease in GVF from about 75 to 50 %, but zonal averages between 50° and 60°N reveal even larger decreases (not shown). A similar decrease, although smaller in magnitude, is observed for 2006-L.

LAI, surface roughness length, and emissivity for CL are shown in Fig. 5(d–f) to show how differences in intraannual variability are transferred to the scaled parameters in WRF.

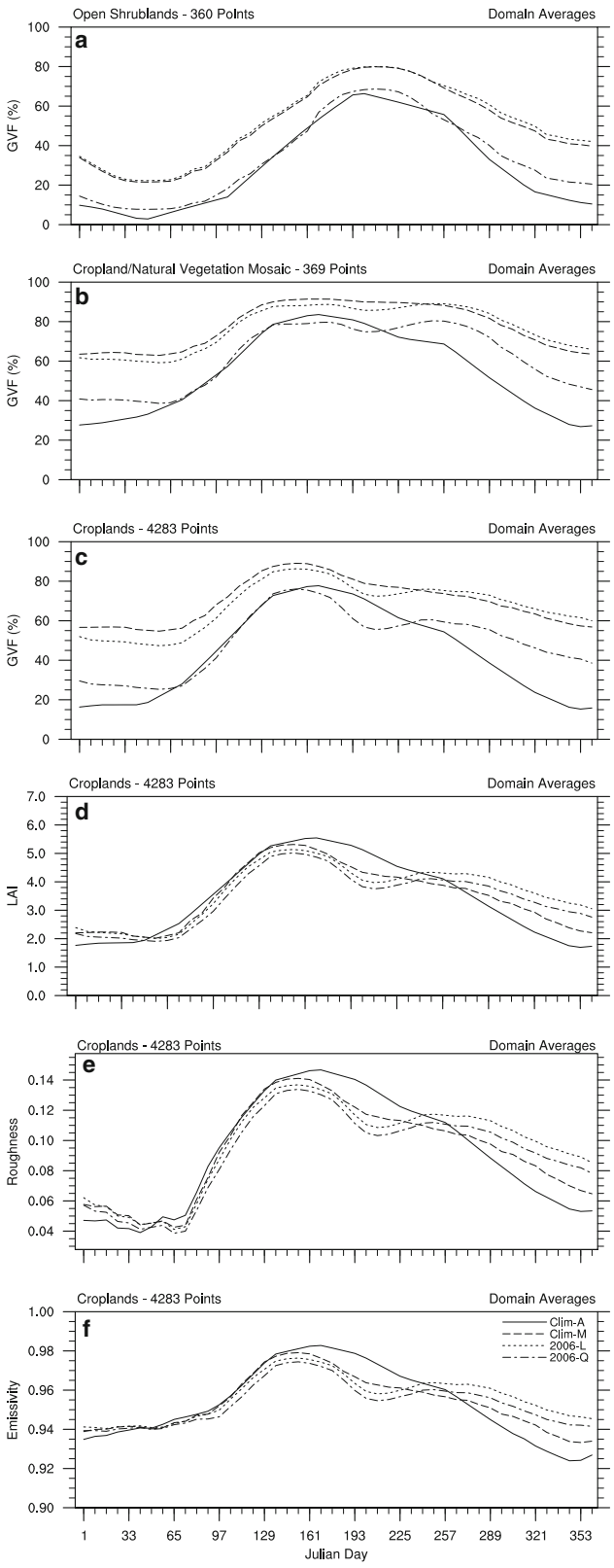

Fig. 5 Comparison of domain-averaged GVF (in percent) for (*a*) open shrublands, (*b*) cropland/natural vegetation, and (*c*) croplands. In addition, (*d*) domain-averaged LAI, (*e*) surface roughness length (in meter), and (*f*) emissivity for croplands sites are shown. Otherwise similar to Fig. 4

Almost identical values are found for the parameters until June, while large differences are found during summer and autumn. The low summer vegetation fraction, accompanied by lowering the LAI value as shown by 2006-Q, significantly reduces the potential for transpiration in the WRF model over croplands.

The spatial distribution of GVF during the heat wave event in July 2006 is shown in Fig. 6. The squares (represented by letters "a" and "b") indicate areas selected for statistical comparison between the numerical simulations and observed values represented by E-OBS (see Section 5). As expected, Clim-M and 2006-L show much higher vegetation fractions, especially in forested areas, compared to Clim-A, while cropland sites are more varied. The 2006-Q map shows much lower vegetation fractions for cropland sites compared to the other GVF representations, especially within the squares over France and Poland and in the UK. The colors indicate differences of the order of 50 % in some areas between Clim-A and 2006-Q. Considering that 2006-Q shows similar seasonal development during springtime compared to Clim-A (see Fig. 5), it is clearly seen how extreme events or changes in management practice can alter the appearance of GVF.

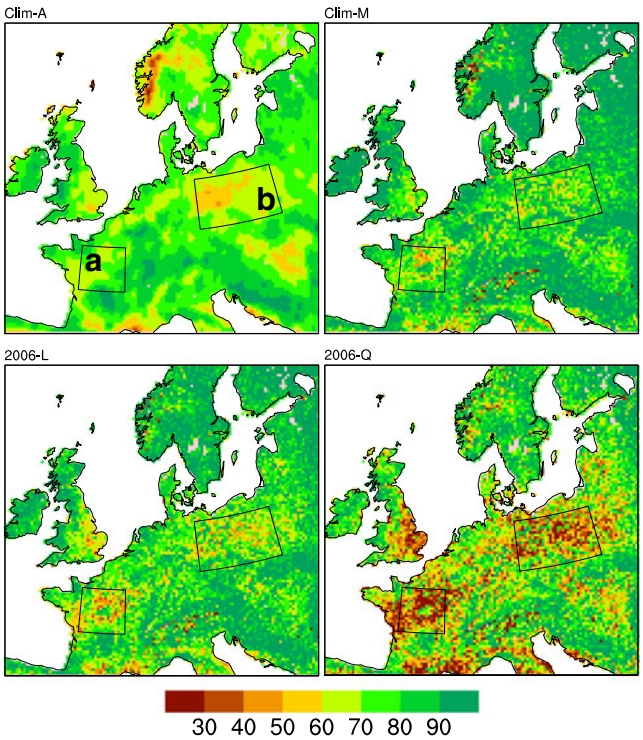

Fig. 6 Comparison of averaged GVF (in percent) from Clim-A, Clim-M, 2006-L, and 2006-Q during July 2006. The areas indicated with *squares* over (*a*) France and (*b*) Poland are used for error statistics in Table 2

5 Results from numerical experiments

To check the validity of our modeling setup, time series of simulated precipitable water (PW), a vertically integrated variable, were compared to observed data obtained from a GPS station in central Germany. The location is close to the center of our domain at 52.30°N, 10.46°E and thus not influenced by the boundary conditions. Only observed and predicted PWs from numerical simulations with Clim-A and Clim-M are shown since nearly identical results are obtained using 2006-L and 2006-Q. A very good correspondence between modeled and observed PW during the whole year is seen (Fig. 7). The differences between the modeled PWs are small and indicate that our simulations describe the temporal evolution of the atmospheric moisture conditions equally well.

The accumulated precipitation fields during March, April, and May obtained from Clim-A and Clim-M are compared to observed precipitation from E-OBS in Fig. 8. 2006-L and 2006-Q are excluded in the comparison since their precipitation fields only deviate slightly from those obtained by the climatologies. Almost identical accumulated precipitation amounts are found between Clim-A and Clim-M, and the precipitation patterns are similar to those in E-OBS, although many regions show higher predicted accumulated values. Other periods of the annual cycle show similar trends (not shown); thus, precipitation is largely controlled by the grid-nudging technique and other physical processes (e.g., microphysics and convection parameterization) and not influenced by changes in GVF.

Mean 2-m temperature fields during March–May are shown in Fig. 9 for Clim-A, Clim-M, and E-OBS. Again, 2006-L and 2006-Q are excluded from the comparison due to their similarity with the climatologies. Clim-A and Clim-M show very similar temperature patterns with only minor differences over the UK, France, and Germany. The patterns are consistent with E-OBS although cold biases of 1–4 K are observed throughout the domain. The largest biases are found in the northern regions, especially over Finland, but decrease towards the south. Minimum and maximum 2-m temperatures show similar spatial trends and biases (not shown).

We focus now on the heat wave period in July (Fig. 10) shows July-averaged 2-m temperatures (in kelvin) for all simulations and E-OBS. The largest differences between the simulated temperatures are seen in areas containing mostly croplands; hence, the northern regions with mainly forest show uniform temperatures. The Clim-A simulation shows higher temperatures over Poland and Hungary, while lower temperatures are found in central France compared to Clim-M. The 2006-L simulated temperatures are similar to those in Clim-M as expected but show higher temperatures over Poland. The warmest temperatures are simulated in

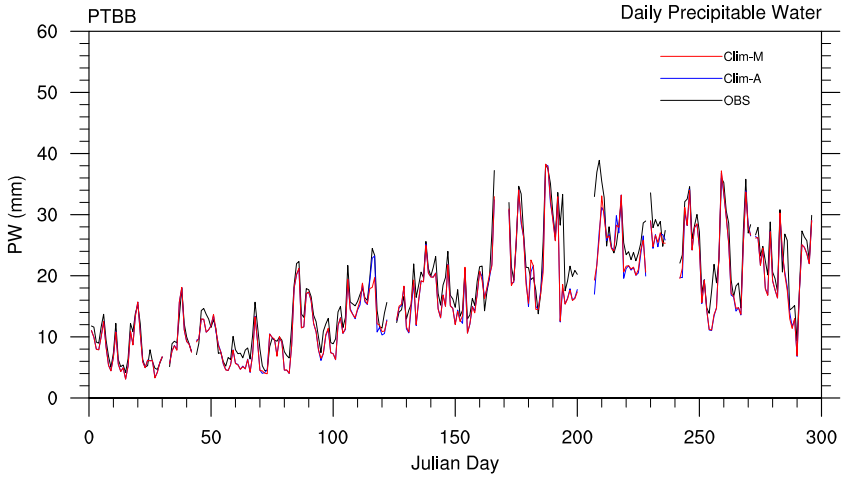

Fig. 7 Comparison of the time series of precipitable water (PW) at station PTBB located in central Germany (52.30°N, 10.46°E). Observed PW is represented in *black* while predicted PW is indicated in *blue* and *red* for Clim-A and Clim-M, respectively

2006-Q compared to the other simulations, especially in central France. All simulations still indicate a cold bias compared to E-OBS.

Differences between the simulated mean 2-m temperatures during July reflect changes in their minimum and maximum 2-m temperatures as well. The differences are shown in Fig. 11 for the 2006 specific simulations and Clim-A. We did not include Clim-M since the results are almost identical to those in 2006-L and Clim-A. 2006-L results in warmer minimum and maximum temperatures over France and southern UK compared to Clim-A, while mostly lower temperatures are indicated in the northern and eastern regions. The differences range from 0 to 2 K. Much larger temperature differences are shown by 2006-Q compared to Clim-A. The northern forested regions show slightly lower temperatures for both minimum and maximum temperatures, while the remaining areas show higher temperatures. In some cases, temperature differences were more than 2 K.

Coefficients of determination (R^2), biases, and root-mean-square errors (RMSEs) of simulated daily mean, maximum, and minimum temperatures against E-OBS values, shown in Table 2, were calculated. The statistics are computed separately in the areas indicated in Fig. 6 (France and Poland) and over the entire model domain. The areas were selected because they show the largest change in GVF among the different data sets. All GVF representations show similar R^2 values with lower values found for minimum temperature. Both bias and RMSEs are significantly improved by 2006-Q compared to Clim-A, showing improvements between 20 and 45 % for mean temperature over Poland and France. Similarly, maximum temperature biases are reduced by 14–31 %, while minimum temperature biases are reduced with more than 45 %. Both Clim-M and 2006-L show lower biases and RMSEs compared to Clim-A over France while poorer performance is obtained over Poland. The statistics show that consistent improvements are obtained using the quadratic method to derive GVF, while the linear approach shows mixed results. Simulated precipitation patterns did not show any sensitivity to changes in vegetation fractions and only small differences in accumulated amounts were found.

Temperature results during the fall showed similar statistics between the model simulations, still with lower temperatures compared to E-OBS. The best performance was shown by Clim-A although the difference to 2006-Q was small.

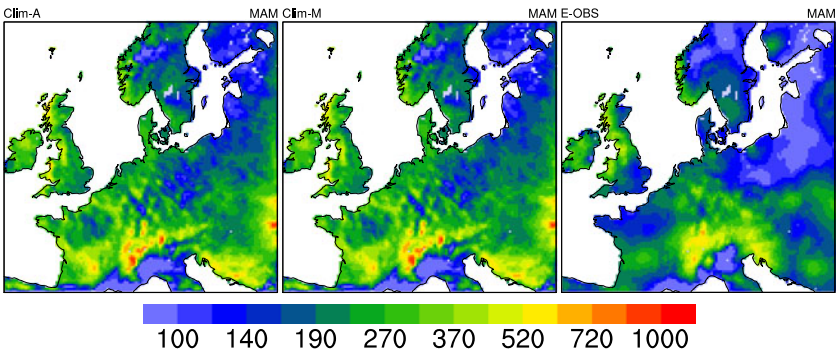

Fig. 8 Accumulated precipitation (in millimeter) for Clim-A, Clim-M, and E-OBS during March, April, and May 2006

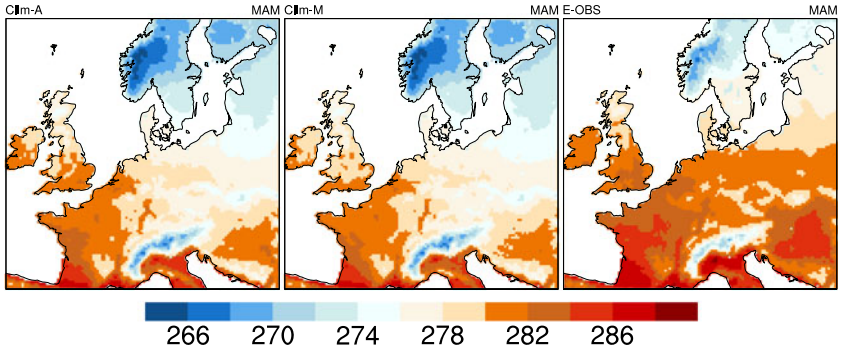

Fig. 9 Mean 2-m temperature (in kelvin) for Clim-A, Clim-M and E-OBS during March, April, and May 2006. Mean temperatures are calculated from $(T_{min} + T_{max})/2$

6 Discussion

The GVF products presented in Figs. 4 and 5 show significant differences in vegetation fractions during the wintertime, while little difference in the prediction of temperature is found due to the low radiation conditions and dormant vegetation. However, too low winter vegetation fractions for ENF are shown by Clim-A since more constant seasonality should be expected (Miller et al. 2006). It is therefore possible that the MODIS-derived GVF products are closer to reality (though 2006-Q possibly still indicates too low values). A comparison of the zonal medians between 50°N–60°N and 60°N–70°N for the MODIS GVF products reveals higher winter vegetation fractions for the southern area, suggesting that the ecosystem-dependent filling, mainly used above 60°N, plays a major role in further improvement of the winter vegetation values.

The temperature differences among the simulations during July (Table 2) are related to changes in the surface energy distribution. Figure 12 shows the differences in sensible and latent heat fluxes between the 2006 specific GVF products and Clim-A during July. Many of the areas covered by croplands show 30 W m^{-2} less latent heat flux for 2006-Q compared to Clim-A, while sensible heat flux is 20 W m^{-2} higher. The residual energy was largely converted into soil heat fluxes (not shown). Similar patterns are seen between 2006-L and Clim-A though the differences are smaller in magnitude. The higher daytime temperatures, specifically shown by 2006-Q, are directly related to the increased sensible heat flux, while higher nighttime temperatures occur due to increased soil temperature leading to higher nighttime ground heat flux into the atmosphere. Since we neither observed large differences in the rootzone soil moisture availability, precipitation, nor cloud cover, the

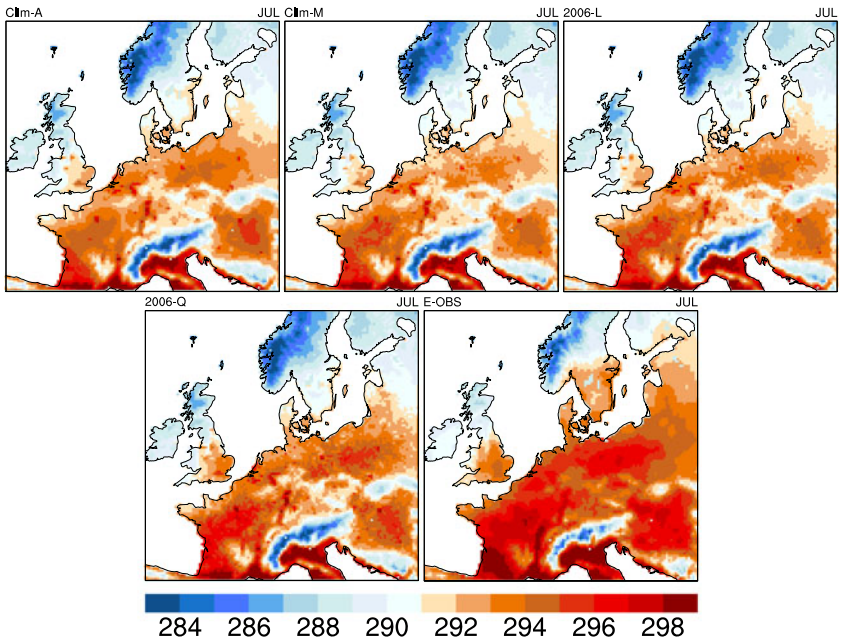

Fig. 10 Mean 2-m temperature (in kelvin) during July 2006 for Clim-A, Clim-M, 2006-L (*upper panel*), 2006-Q and E-OBS (*lower panel*). Mean daily temperatures are calculated from $(T_{min} + T_{max})/2$

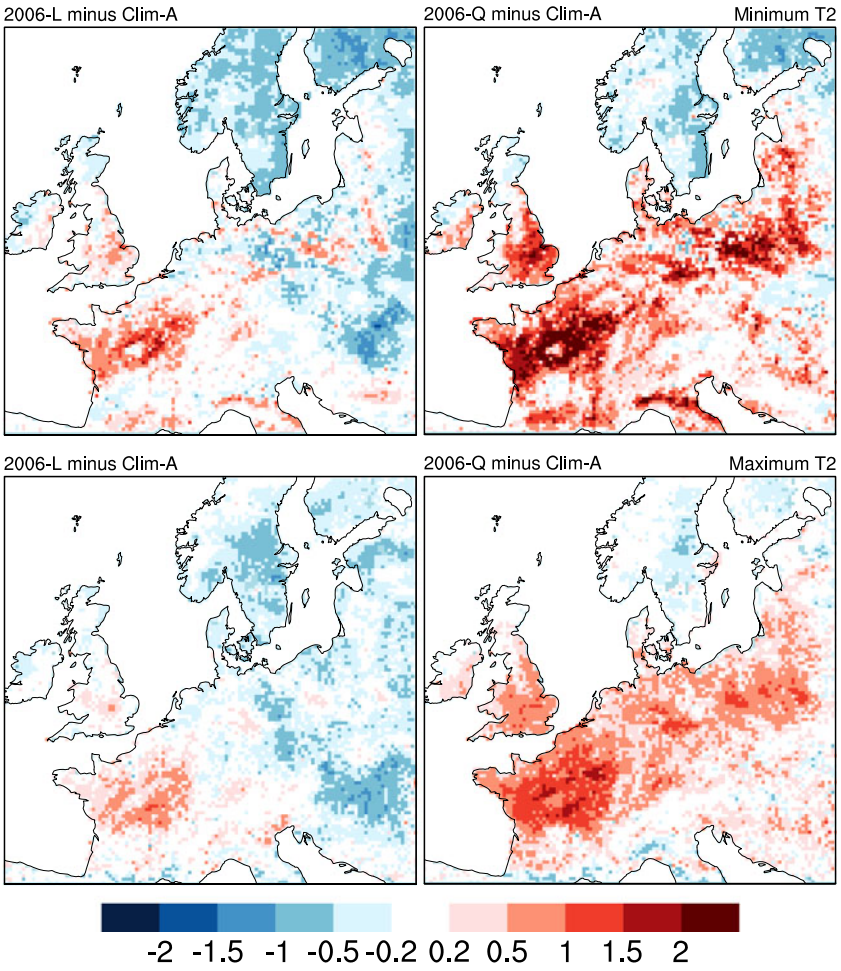

Fig. 11 Difference plots of 2006-L (*left column*) and 2006-Q (*right column*) minus Clim-A for averaged daily minimum 2-m temperature (*upper row*) and maximum daily 2-m temperature (*lower row*) during July 2006. Units are in kelvin

Table 2 Coefficients of determination, Bias and RMSE of 2006 July daily mean, maximum and minimum temperatures from Clim-A, Clim-M, 2006-L and 2006-Q against E-OBS values over the areas enclosed by squares in Fig. 6 and for the whole domain

Simulation	Mean			Max			Min		
	R^2	Bias	RMSE	R^2	Bias	RMSE	R^2	Bias	RMSE
France									
Clim-A	0.77	−2.78	2.97	0.82	−3.45	3.73	0.62	−2.17	2.55
Clim-M	0.80	−2.57	2.75	0.84	−3.30	3.56	0.64	−1.88	2.31
2006-L	0.81	−2.32	2.53	0.84	−3.06	3.34	*0.66*	−1.63	2.12
2006-Q	*0.82*	*−1.53*	*1.88*	*0.86*	*−2.37*	*2.69*	0.64	*−0.75*	*1.71*
Poland									
Clim-A	0.75	−2.51	2.85	0.70	−3.56	3.99	*0.58*	−1.43	2.37
Clim-M	0.75	−3.17	3.44	0.70	−4.22	4.59	0.57	−2.09	2.84
2006-L	0.75	−2.73	3.05	0.70	−3.80	4.20	0.57	−1.63	2.55
2006-Q	*0.78*	*−1.91*	*2.33*	*0.73*	*−3.04*	*3.49*	0.57	*−0.75*	*2.14*
Domain									
Clim-A	0.82	−2.14	2.13	0.82	−2.75	2.69	0.67	−1.52	2.11
Clim-M	0.80	−2.41	2.33	0.80	−3.02	2.89	0.66	−1.79	2.29
2006-L	0.81	−2.28	2.24	0.81	−2.90	2.80	0.67	−1.66	2.21
2006-Q	*0.83*	*−1.87*	*1.95*	*0.83*	*−2.50*	*2.50*	*0.69*	*−1.22*	*2.01*

The squares are named after their location over France and Poland. The best error statistics for each area are indicated in italics. Units are in kelvin

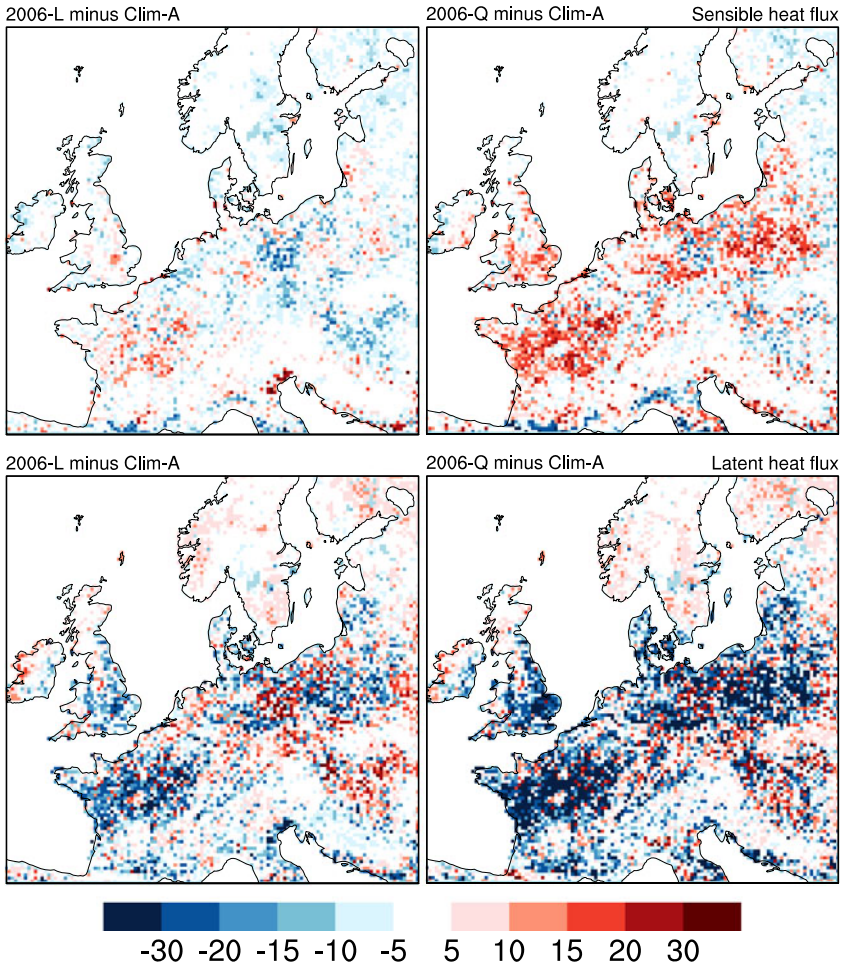

Fig. 12 Difference plots of 2006-L (*left column*) and 2006-Q (*right column*) minus Clim-A for July 2006 averaged sensible heat fluxes (*upper row*) and latent heat fluxes (*lower row*). The fluxes are defined as positive upwards in units of watts per square meter

altered surface energy distribution is mainly due to direct changes in GVF.

The quadratic MODIS GVF product clearly shows the best performance in terms of temperature simulation compared to the linear products at low-resolution WRF model simulations. However, this does not necessarily ensure better results at high resolution. The very similar range in vegetation fractions shown by the AVHRR data and the high-resolution quadratic GVF data, aggregated to low resolution through WPS, is encouraging. It suggests that good performance across spatial scales might be expected using the quadratic GVF product. Furthermore, the quadratic NDVI to GVF relation was recently recommended by Montandon and Small (2008) to avoid large overestimations of GVF due to underestimation of bare soil NDVI. They showed that the maximum error would occur for NDVI values in the range of $0.2 \leq N \leq 0.4$, which typically are found during winter or spring, e.g., for croplands. This critical range was also reached during the 2006 summer heat wave for croplands; thus, overestimation of vegetation fraction during this period is minimized with the quadratic relationship. In addition, the use of local scenes was also recommended to minimize underestimation of N_s, as was done in this study.

The results of simulation with a limited-area coupled land–atmosphere model have several sources of error, including both boundary forcing and modeled sub-grid physical processes that use many parameters. The contribution to model error from physical processes has been investigated in previous studies. For example, Decharme et al. (2009) found that more advanced parameterization of the land surface hydrology over West Africa affected surface temperature through alteration of the surface fluxes. However, they noted that more realistic vegetation properties should have been used in their study, which, additionally, would have impacted the surface fluxes. Mooney et al. (2013) found that radiation and PBL schemes influence the surface temperature predictions, although these predictions mostly were affected by the choice of LSM. Primarily cold biases over Europe were found using the Noah LSM, while another LSM showed large positive biases. The cold temperature bias compared to E-OBS shown in

the present study was also reported by García-Díez et al. (2012). They simulated the atmospheric conditions over Europe during 2002 using the ERA-Interim reanalysis data and by applying different PBL schemes. The simulations were done in a reforecast mode using 12 h of spin-up. Their results and the present study eliminate the use of CFSR data and the MYJ PBL scheme as main causes of the overall temperature cold bias. The main problem could be related to the radiative balance (Manning et al. 2010; García-Díez et al. 2012) which was only slightly changed by updating the GVF data. Therefore, future investigations of the impact of remotely sensed albedo on temperature in WRF/Noah should be carried out using a similar approach to this study. The advantages are that the grid-nudging technique minimizes changes in precipitation and cloud cover and the continuous simulation avoids reinitialization of soil moisture, which is important for the surface energy balance.

The longer growing season indicated by the new GVF data is perhaps a result of higher autumn temperatures over the northern latitudes during the last two decades that, additionally, have lead to increases in photosynthesis and respiration (Piao et al. 2008). However, the increased climate variability predicted by climate models (Seneviratne et al. 2006) could significantly alter the interannual variability of GVF, suggesting that concurrent land cover characteristics will be more important for climate predictions in the future. A key process in the approach presented in this paper is the development of a NDVI climatology. Besides introducing a robust way of treating missing data and bad pixel values, it offers attractive perspectives for future studies. The new NDVI climatology ensures an efficient way to fill annual GVF data sets and can be used for both climate and seasonal forecasting purposes. In addition, it can be used in a real-time system to extrapolate the current vegetation conditions to the short-term future using a "deviation from climatology" method.

7 Conclusions

A statistically robust MODIS-derived NDVI climatology, reflecting recent landuse and climatic changes, was derived to enable computation of concurrent GVF information. To ensure high quality of the climatology, existing and novel data-processing techniques were applied on 10 years of NDVI images. A GVF climatology and two single-year representations of GVF, using both linear and quadratic NDVI to GVF relations, were derived and used in WRF model simulations over Europe for the 2006 heat wave year at 18-km grid spacing.

The GVF seasonality for the most common landuse classes in the European domain showed that the linear MODIS GVF products generally resulted in higher vegetation fractions compared to the AVHRR GVF data, while the quadratic GVF product showed very good agreement with the magnitude and annual range of the AVHRR data. Vegetation stresses related to the 2006 heat wave or changes in management practice for croplands were clearly indicated by the 2006 specific GVF products. Additionally, prolonged autumnal growth periods were indicated by the new GVF products for mainly deciduous forests types.

The output from the numerical simulations was compared to E-OBS daily gridded observational data. Comparison during the spring showed that all simulations produced equally good results. However, temperatures during July were consistently improved by the 2006 quadratic GVF product compared to E-OBS, reducing the mean temperature bias by 0.60–1.25 °C (20–45 %) in areas severely affected by heat wave conditions. The reduction in bias over the whole domain was 0.27 °C (10 %). Improvements for minimum temperature were larger than those obtained for maximum temperature. The linearly derived MODIS GVF products showed varying results and did not perform as good as the quadratic GVF product during the heat wave period. The results from a limited-area coupled land–atmosphere model have several potential sources of error, including the representation of the land surface. This study has shown that specification of observed vegetation properties in a year that deviates significantly from normal can improve predicted near-surface states.

Acknowledgments The study took place within the framework of the research project "Implementing Earth observations, advanced satellite based atmospheric sounders and distributed temperature sensing for effective land surface representation in water resource modelling" (2009–2013) financed by the Danish Research Council (project no. 274-08-0380). We thank the online Data Pool at the NASA Land Processes Distributed Active Archive Center (LP DAAC), USGS/Earth Resources Observation and Science (EROS) Center, Sioux Falls, South Dakota (http://lpdaac.usgs.gov/get_data) for making the MODIS data available and the ECA&D project (http://eca.knmi.nl) within the EU-FP6 project ENSEMBLES (http://www.ensembles-eu.org) for providing the E-OBS data.

References

Bruyninx C (2004) The EUREF Permanent Network: a multidisciplinary network serving surveyors as well as scientists. GeoInformatics 7:32–35

Chen F, Dudhia J (2001) Coupling an advanced land surface-hydrology model with the Penn State-NCAR MM5 modeling system. Part II: preliminary model validation. Mon Weather Rev 129(4):587–604

Chen J, Jonsson P, Tamura M, Gu Z, Matsushita B, Eklundh L (2004) A simple method for reconstructing a high-quality NDVI time-series data set based on the Savitzky-Golay filter. Remote Sens Environ 91(3–4):332–334

Chen F, Manning K, Lemone M, Trier S, Alfieri J, Roberts R, Tewari M, Niyogi D, Horst T, Oncley S, Basara J, Blanken P (2007) Description and evaluation of the characteristics of the NCAR high-resolution land data assimilation system. J App Meteorol Climatol 46:694–713

Decharme B, Ottlé C, Saux-Picart S, Boulain N, Cappelaere B, Ramier D, Zribi M (2009) A new land surface hydrology within the Noah-WRF land-atmosphere mesoscale model applied to semiarid environment: evaluation over the Dantiandou Kori (Niger). Advanc Meteorolog. doi:10.1155/2009/731874. article ID 731874

Della-Marta PM, Haylock MR, Luterbacher J, Wanner H (2007) Doubled length of western European summer heatwaves since 1880. J of Geophys Res 112:D15103. doi:10.1029/2007JD008510

Didan K, Huete A (2006) MODIS vegetation index product series: collection 5 change summary. Tech rep

Dudhia J (1989) Numerical study of convection observed during the winter monsoon experiment using a mesoscale two-dimensional model. J Atmos Sci 46(20):3077–3107

Friedl MA, McIver DK, Hodges JCF, Zhang XY, Muchoney D, Strahler AH, Woodcock CE, Gopal S, Schneider A, Cooper A, Baccini A, Gao F, Schaaf C (2002) Global land cover mapping from MODIS: algorithms and early results. Remote Sens Environ 83:287–302

García-Díez M, Fernández J, Fita L, Yague C (2012) Seasonal dependence of WRF model biases and sensitivity to PBL schemes over Europe. QJR Meteorol Soc 139:501–514. doi:10.1002/qj.1976

Gu J, Li X, Huang C, Okin G (2009) A simplified data assimilation method for reconstructing time-series MODIS NDVI data. Adv Space Res 44(4):501–559

Gutman G, Ignatov A (1998) The derivation of the green vegetation fraction from NOAA/AVHRR data for use in numerical weather prediction models. Int J Remote Sens 19(8):1533–1543. doi:10.1080/014311698215333

Haylock MR, Hofstra N, Klein Tank AMG, Klok EJ, Jones PD, New M (2008) A European daily high-resolution gridded data set of surface temperature and precipitation for 1950–2006. J Geohys Res 113:D20119

Hofstra N, Haylock M, New M, Jones P (2009) Testing E-OBS European high-resolution gridded data set of daily precipitation and surface temperature. J Geophys Res 114:D21101. doi:10.1029/009JD011799

Hong SY, Dudhia J, Chen SH (2004) A revised approach to ice-microphysical processes for the bulk parameterization of cloud and precipitation. Mon Weather Rev 132(1):103–120

Hong S, Lakshmi V, Small E, Chen F, Tewari M, Manning K (2009) Effects of vegetation and soil moisture on the simulated land surface processes from the coupled WRF/Noah model. J Geophys Res 114:D18118. doi:10.1029/208JD011249

Janjic ZI (1996) The surface layer in the NCEP Eta model. Am Met Soc:354–355

Janjic ZI (2002) Nonsingular implementation of the Mellor-Yamada level 2.5 scheme in the NCEP Meso model. Office note 437, NCEP

Jiang L, Kogan F, Guo W, Tarpley JD, Mitchell K, Ek M, Tian Y, Zheng W, Zou C, Ramsay B (2010) Real-time weekly global green vegetation fraction derived from advanced very high resolution radiometer-based NOAA operational global vegetation index (GVI) system. J Geophys Res 115:D11114. doi:10.1029/2009JD013204

Jonsson P, Eklundh L (2002) Seasonality extraction by function fitting to time-series of satellite sensor data. IEEE Trans Geosci Remote Sens 40(8):1824–183

Kain JS (2004) The Kain Fritsch convective parameterization: an update. J Appl Meteorol 43(1):170–181

Kyselý J, Plavcová E (2010) A critical remark on the applicability of E-OBS European gridded temperature data set for validating control climate simulations. J Geophys Res 115:D23118. doi:10.1029/2010JD014123

Lakshmi V, Hong S, Small E, Chen F (2011) The influence of the land surface on hydrometeorology and ecology: new advances from modeling and satellite remote sensing. Hydrol Res 42(2–3): 95–112. doi:10.2166/nh.211.071

Lovell J, Graetz R (2001) Filtering the pathfinder AVHRR Land NDVI data for Australia. Int J Rem Sens 13(22):2649–2654

Ma M, Veroustraete F (2004) Reconstructing pathfinder AVHRR Land NDVI time series data for the northwest of China. Adv Space Res 37(3-4):835–80

Manning K, Tewari M, Barlage M, Chen F, Salamanca F, Martill A (2010) Updates to the Noah LSM in WRF version 3.2. In: 11th WRF users' workshop, NCAR, Boulder, CO

Miller J, Barlage M, Zeng X, Wei H, Mitchell K, Tarpley D (2006) Sensitivity of the NCEP/Noah land surface model to the MODIS green vegetation fraction data set. Geophys Res Lett 33. doi:10.1029/2006L026636

Mlawer EJ, Taubman SJ, Brown PD, Iacono MJ, Clough SA (1997) Radiative transfer for inhomogeneous atmospheres: RRTM, a validated correlated-k model for the longwave. J Geophys Res 102(D14):16,663–16,682. doi:10.1029/97JD00237

Montandon L, Small E (2008) The impact on soil reflectance on the quantification of the green vegetation fraction from NDVI. Rem Sens of Environ 112:1835–1845

Montandon L, Fall S, Pielke RASr, Niyogi D (2011) Distribution Of landscape types in the global historical climatology network. Earth Interact 15:1–22

Moody EG, King MD, Platnick S, Schaaf C, Gao F (2005) Spatial complete global spectral surface albedos: value-added datasets derived from Terra MODIS land products. IEEE Trans Geosci Remote Sens 43(1):144–158

Mooney PA, Mulligan FJ, Fealy R (2013) Evaluation of the sensitivity of the weather research and forecasting model to parameterization schemes for regional climates of Europe over the period 1990–95. J Climate 26:1002–1017

Piao S, Ciais P, Friedlingstein P, Peylin P, Reichstein M, Luyssaert S, Margolis H, Fang J, Barr A, Chen A, Grelle A, Hollinger DY, Laurila T, Lindroth A, Richardson AD, Vesala T (2008) Net carbon dioxide losses of northern ecosystems in response to autumn warming. Nat 451(7174):49–52. doi:10.1038/nature06444

Pielke R (2001) Influence of the spatial distribution of vegetation and soils on the prediction of cumulus convective rainfall. Rev Geophys 39:151–177

Pielke R, Adegoke J, Beltran-Przekurat A, Hiemstra C, Lin J, Nair U, Niyogi D, Nobis T (2007) An overview of regional land use and cover impacts on rainfall. Tellus 59B:587–601

Rebetez M, Dupont O, Giroud M (2009) An analysis of the July 2006 heatwave extent in Europe compared to the record year of 2003. Theor Appl Climatol 95:1–7. doi:10.1007/s00704-007-0370-9

Reynolds RW, Smith T, Liu C, Chelton D, Casey K, Schlax M (2007) Daily high-resolution blended analyses for sea surface temperature. J Climate 20:5473–549

Roerink G, Menenti M, Verhoef W (2000) Reconstructing cloud-free NDVI composites using Fourier analysis of time series. Int J Rem Sens 21(9):1911–1917

Saha S, Moorthi S, Pan HL, Wu X, Wang J, Nadiga S, Tripp P, Kistler R, Woollen J, Behringer D, Liu H, Stokes D, Grumbine R, Gayno G, Wang J, Hou YT, ya Chuang H, Juang HMH, Iredell M, Treadon R, Kleist D, Delst PV, Keyser D, Derber J, Ek M, Meng J, Wei H, Yang R, Lord S, van den Dool H, Kumar A, Wang W, Long C, Chelliah M, Xue Y, Huang B, Schemm JK, Ebisuzaki W, Lin R, Xie P, Chen M, Zhou S, Higgins W, Zou CZ, Liu Q, Chen Y, Han Y, Cucurull L, Reynolds RW, Rutledge G, Goldberg M

(2010) The NCEP climate forecast system reanalysis. Bull Amer Meterol Soc 91:1015–1057

Seneviratne S, Luethi D, Litschi M, Schr C (2006) Land-atmosphere coupling and climate change in Europe. Nat 443:205–209

Skamarock WC, Klemp JB, Dudhia J, Gill DO, Barker M, Duda KG, Huang XY, Wang W, Powers JG (2008) A description of the advanced research WRF version 3. Tech rep, National Center for Atmospheric Research

Stauffer D, Seaman N (1990) Use of four-dimensional data assimilation in a limited-area mesoscale model. Part I: experiments with synoptic-scale data. Mon Weather Rev 110:1250–1277

Stull RB (1988) An introduction to boundary layer meteorology. Kluwer, Dordrecht

Teuling A, Seneviratne S, Stckli R, Reichstein M, Moors E, Ciais P, Luyssaert S, van den Hurk S, Ammann C, Bernhofer C, Dellwik E, Gianelle D, Gielen B, Grnwald T, Klumpp K, Montagnani L, Moureaux C, Sottocornola M, Wohlfahrt G (2010) Contrasting response of European forest and grassland energy exchange to heatwaves. Nat Geosci 3:722–727

Verhoef W, Menenti M, Azzall S (1996) A color composite of NOAA-AVHRR based on time series (1981–1992). Int J Rem Sens 17:231–225

Viovy N, Arino O, Belward A (1992) The Best Index Slope Extraction (BISE): a method for reducing noise in NDVI time-series. Int J Remote Sens 13:1585–1590. doi:10.1080/0143119208904212

Weckwerth T, Parsons D, Koch S, Moore J, Lemone M, Demoz B, Flamant C, Geerts B, Wang J, Feltz W (2004) An overview of the International H2O Project (IHOP2002) and some preliminary highlights. Bull Am Meteorol Soc 85(2):253–277. doi:10.1175/BAMS85-2-253

Yuan H, Dai Y, Xiao Z, Ji D, Shangguan W (2011) Reprocessing the MODIS Leaf area index products for land surface and climate modelling. Remote Sens Environ 115(5):1171–1187. doi:10.1016/j.rse.2011.01.001

Zeng X, Dickinson RE, Walker A, Shaikh M, DeFries RS, Qi J (2000) Derivation and evaluation of global 1-km fractional vegetation cover data for land modeling. J Appl Meteorol 39:826–839